CSF contamination-invariant statistics in conventional diffusion-weighted MRI of the fornix

Arkesteijn, Joor; Poot, Dirk; de Groot, M; Ikram, M A; Niessen, Wiro; van Vliet, Lucas; Vernooij, MW; Vos, Frans

DOI
10.1088/2057-1976/aa890e

Publication date
2017

Document Version
Final published version

Published in
Biomedical Physics & Engineering Express

PAPER

CSF contamination-invariant statistics in conventional diffusion-weighted MRI of the fornix

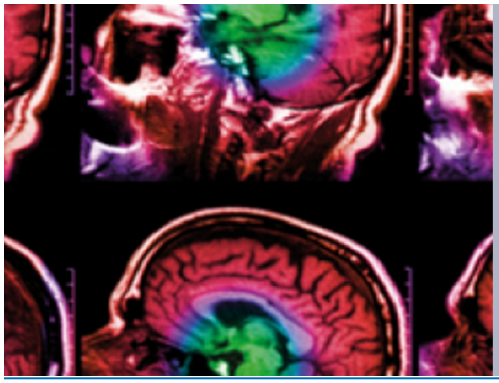

Biomedical Physics & Engineering Express

PAPER

CSF contamination-invariant statistics in conventional diffusion-weighted MRI of the fornix

G A M Arkesteijn[1,2,3], D H J Poot[1,2,3], M de Groot[2,3,4], M A Ikram[3,4], W J Niessen[1,2,3], L J van Vliet[1], M W Vernooij[3,4] and F M Vos[1,5,6]

[1] Quantitative Imaging Group, Department of Imaging Physics, Delft University of Technology, Delft, The Netherlands
[2] Dept. of Medical Informatics, Erasmus MC, Rotterdam, The Netherlands
[3] Dept. of Radiology and Nuclear medicine, Erasmus MC, Rotterdam, The Netherlands
[4] Dept. of Epidemiology, Erasmus MC, Rotterdam, The Netherlands
[5] Dept. of Radiology, Academic Medical Center, University of Amsterdam, Amsterdam, The Netherlands
[6] Author to whom any correspondence should be addressed.

E-mail: f.m.vos@tudelft.nl

Keywords: DTI, DW-MRI, partial volume effects

RECEIVED
17 July 2017

REVISED
16 August 2017

ACCEPTED FOR PUBLICATION
30 August 2017

PUBLISHED
17 November 2017

Abstract

The goal of this paper is to develop a method for assessment of microstructural properties of the fornix in conventional (low resolution, single non-zero *b*-value) diffusion-weighted magnetic resonance imaging (DW-MRI) data. For this purpose, a bi-tensor model, comprising of an isotropic and an anisotropic diffusion compartment, was fitted to the diffusion-weighted images. Two subject-specific constraints were studied to solve the ill-posedness of the parameter estimation at a single (non-zero) *b*-value, namely by fixating the mean diffusivity (MD) or the axial diffusivity (AxD) of the anisotropic compartment. The bi-tensor statistics were compared to conventional diffusion statistics using simulated fiber bundles with different diameters and using fornix segmentations of 577 elderly subjects. Based on simulated fiber bundles, the anisotropy (FA) estimated by the bi-tensor model did not become biased with decreasing fiber bundle diameter, unlike conventional diffusion statistics such as FA and MD estimated by the single tensor model. In the population-based study, the bi-tensor tissue fraction decreased significantly with age, suggesting an increase of free water. The FA estimated by the bi-tensor model decreased with age, but this relation was not significant when the subject-specific values to which MD or AxD were constrained were added as covariates in the regression analysis. The distinction of an isotropic and an anisotropic diffusion compartment may allow a more sophisticated analysis of the fornix based on conventional DW-MRI data.

1. Introduction

Diffusion-weighted magnetic resonance imaging (DW-MRI) is a non-invasive imaging technique in which image contrast is determined by the (hindered) molecular diffusion of water (Stejskal and Tanner 1965). DW-MRI is frequently used to study the brain's white matter, because the diffusion behavior of water reflects the orientation and organization of neural fibers in the white matter (Beaulieu 2002).

Diffusion tensor imaging (DTI) is a popular application of DW-MRI, in which the diffusion behavior is modeled by a rank-two diffusion tensor (Basser *et al* 1994). In voxels containing a single tissue type, DTI provides tissue-specific measures of the microstructure. However, in voxels containing different tissue classes due to partial volume effects (PVEs), the diffusion tensor is influenced by all these diffusion compartments (Alexander *et al* 2001).

PVE complicate the analysis of diffusion-weighted images (DWIs) in two ways. Firstly, PVE make diffusivity statistics sensitive to random processes such as the positioning of the image grid. This random process yields a varying voxel composition, which causes additional noise on all diffusivity statistics, thereby decreasing the sensitivity to detect microstructural change. Secondly, PVE can introduce a bias in diffusivity statistics that depends on the size, structure and shape of the involved tracts or objects. DTI metrics such as the mean diffusivity (MD) and fractional

anisotropy (FA) of the diffusion tensor may therefore be modulated by macrostructural properties such as fiber bundle thickness (Vos *et al* 2011).

Cerebrospinal fluid (CSF) contamination is a PVE that occurs when both CSF and tissue contribute to the signal of the same voxel. CSF is characterized by unhindered diffusivity with an apparent *in vivo* diffusion coefficient approximately equal to that of free-water at 37 °C (Alexander *et al* 2001). The increased isotropic diffusion in CSF contaminated white matter voxels results in an overestimation of MD and an underestimation of FA. Therefore, increasing degrees of CSF contamination driven by macrostructural effects such as white matter atrophy may incorrectly suggest or exaggerate microstructural change (Metzler-Baddeley *et al* 2014). The fornix, the primary white matter bundle connecting the hippocampus to the mammillary bodies of the hypothalamus, is particularly prone to CSF contamination due to its small size and proximity to the third and lateral ventricles (Concha *et al* 2005). Given its importance to episodic memory (Aggleton *et al* 2000, Metzler-Baddeley *et al* 2011) it is a good example of the challenge to disentangle the macroscopic effect of increasing CSF contamination due to aging from 'true' changes in fornix microstructure.

Different techniques can be used to limit the effects of CSF contamination. CSF contamination can be reduced during acquisition by either using a higher spatial resolution or suppressing the CSF signal with a fluid-attenuated inversion recovery (FLAIR) sequence (Papadakis *et al* 2002, Chou *et al* 2005, Concha *et al* 2005). However, (obviously) these methods are not be applicable to already acquired image databases applying conventional diffusion imaging protocols.

Several studies have proposed to include measures of brain atrophy or brain size as covariates in regression analyzes to account for PVE by CSF. Examples are the inclusion of intracranial volume (Takao *et al* 2011), brain parenchymal fraction (Rashid *et al* 2004), or white matter fraction (Vernooij *et al* 2008). However, these global measures are not necessarily optimal to correct for local effects such as CSF contamination in the fornix (Metzler-Baddeley *et al* 2012). Local measures reflecting fornix atrophy, e.g. fornix volume or cross-sectional area, may be more appropriate to correct for CSF contamination in the fornix. However, such corrections cannot easily take morphological properties into account, such as fiber bundle shape, orientation or curvature, which may also modulate DTI metrics (Vos *et al* 2011).

Preferably, CSF contamination is corrected on a voxel-by-voxel basis by explicitly modeling the contribution of CSF in the DW-MRI signal (Metzler-Baddeley *et al* 2012). A model-based approach for CSF decontamination using a two-compartment tensor model was proposed in (Pierpaoli and Jones 2004). Ideally, the intra-axonal and extra-cellular water in the tissue microstructure are also modeled with separate diffusion compartments such that the overall system is modeled as a three-compartment system (intra-axonal, extra-cellular and CSF) (Zhang *et al* 2012). However, for a stable fit of these models, the DWIs have to be acquired with multiple diffusion weightings (*b*-values) (Pasternak *et al* 2009, Hoy *et al* 2014) at the expense of a longer imaging time. Unfortunately, in many datasets of interest (such as the ADNI data (Jack *et al* 2010) or the Rotterdam Scan Study (Ikram *et al* 2015)) the diffusion data has already been acquired using a conventional single (non-zero) *b*-value acquisition protocol.

In case of conventional single (non-zero) *b*-value DWIs, the fit of a simple two-compartment model is ill-posed. Prior work has attempted to make the estimation problem well-posed by spatially regularizing the diffusion tensor of the anisotropic compartment (Pasternak *et al* 2009). However, recent work has shown that such a spatial regularization does not actually alleviate the degeneracy of the estimation problem (Taquet *et al* 2015). To make the estimation well-posed, a later work globally constrained the MD of the anisotropic compartment (Arkesteijn *et al* 2015). This approach resulted in statistics with a reduced sensitivity to PVE with CSF. However, a limitation of this work was that a global constraint may not be appropriate for every subject, which in turn may introduce an estimation bias.

The goal of this paper is to develop a method for assessment of structural properties of the fornix in conventional (low resolution, single non-zero *b*-value) diffusion-weighted MRI data. In particular, the method targets analysis of diffusion data from a large population study (Hofman *et al* 2015). Instead of using global (population-averaged) constraints to make estimation of a two-compartment model feasible as in (Arkesteijn *et al* 2015), we use subject-specific constraints on the axial diffusivity (AxD) or MD of the anisotropic compartment. We provide an extensive evaluation by investigating the macrostructural dependence of conventional and proposed diffusion statistics using in-silico simulation. Furthermore, the reproducibility of conventional as well as proposed diffusion statistics is determined on 20 subjects for whom rescan data was available. Finally, the effects of ageing on both conventional and proposed diffusion statistics of the fornix are investigated on a large (population) dataset of 577 subjects.

2. Methods

2.1. Bi-tensor model

We use a bi-tensor representation to model the DW-MRI data (Pasternak *et al* 2009). A more advanced approach using a three-compartment model (intra-axonal water, extra-cellular water and CSF) as in (Zhang *et al* 2012) is not feasible with our data. The bi-tensor representation assumes a CSF-contaminated voxel to consist of two diffusion compartments: a tissue

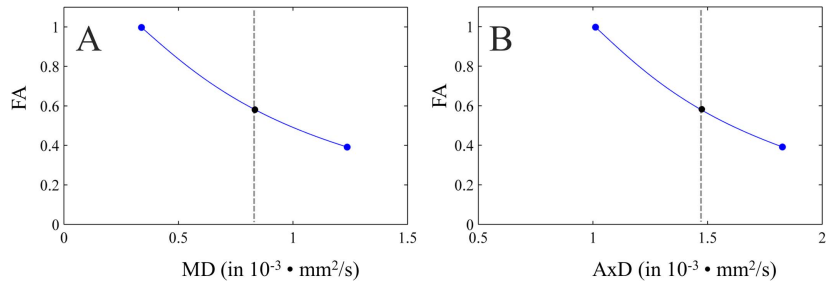

Figure 1. Visualization of a degenerate set of diffusion tensors. (A) FA versus the mean diffusivity (MD) of the diffusion tensor. (B) FA versus the axial diffusivity (AxD) of the diffusion tensor. The introduction of a constraint, e.g. on the MD or the AxD, allows a single diffusion tensor from this degenerate set to be constructed.

compartment and a CSF compartment. The diffusion signal originating from these compartments can be modeled as a weighted sum of both diffusion signals. The diffusion in the tissue compartment is assumed to be Gaussian. The water in the CSF compartment is expected to diffuse freely, which at 37 °C can be modeled by an isotropic diffusion tensor with eigenvalues equal to $d_{\mathrm{CSF}} = 3.0 \times 10^{-3}\,\mathrm{mm^2\,s^{-1}}$. The bi-tensor signal model is formulated as:

$$S(b, \mathbf{g}) = S_0(f\exp(-b\mathbf{g}^T\mathbf{D}\mathbf{g}) + (1-f)\exp(-bd_{\mathrm{CSF}})), \quad (1)$$

where b is the experimental parameter that represents the amount of diffusion-weighting, $\mathbf{g}$ is a unit vector that specifies the direction of a diffusion-encoding gradient pulse, S_0 is the volume-weighted average of the non-diffusion weighted signals from the CSF and tissue compartment, f and $(1-f)$ are the signal fractions of the tissue and CSF compartments respectively, and $\mathbf{D}$ is the diffusion tensor of the tissue compartment. When the DWIs have been acquired at two or more different (non-zero) b-values, the unknown parameters S_0, f and $\mathbf{D}$ can be estimated by minimizing a distance function between the model and the measured diffusion signal. However, when the DWIs have been acquired at a single b-value, different combinations of f and $\mathbf{D}$ exist that result in the same predicted diffusion signal. This makes the inverse problem of estimating the unknown parameters ill-posed.

2.2. CSF contamination-invariant statistics

The degenerate (f, $\mathbf{D}$) pairs can be found by setting the tissue fraction f to different values in the interval from 0 to 1, while estimating the remaining unknown parameters by fitting equation (1) to the observed data. Let $\mathbf{\Omega}$ be the set of all positive-definite diffusion tensors $\mathbf{D}$ that are obtained as such. The degenerate set $\mathbf{\Omega}$ can be visualized by, for instance, plotting the FA against the MD for all diffusion tensors in $\mathbf{\Omega}$ (example in figure 1(A)), or by plotting the FA versus the AxD (example in figure 1(B)). Figure 1(A) illustrates how the exact same signal profile can be obtained by reducing the FA and increasing the MD of tensor $\mathbf{D}$; at the same time the volume fraction of the isotropic part $(1-f)$ decreases for compensation (not shown in the figure). Alternatively, figure 1(B) shows how an identical signal profile is obtained by lowering FA and increasing AxD, also at a simultaneously lower $(1-f)$. Unfortunately, without additional information, the true diffusion tensor modeling the tissue compartment cannot be reconstructed.

To better characterize the true diffusion tensor $\mathbf{D}$, we will study two different approaches to select a tensor from a degenerate set. In the first approach, we select a tensor with a fixed MD; in the second approach, we select a tensor with a fixed AxD. In figure 1 it is illustrated how both approaches select a unique diffusion tensor from the degenerate set, and hence yield a well-posed estimation problem. It should be noted that these tensors can be efficiently computed by constraining the diffusion tensor during the fitting of the model. In previous work, a global value (same for all subjects) of $8.0 \times 10^{-3}\,\mathrm{mm^2\,s^{-1}}$ was used as a constraint for the MD (Arkesteijn *et al* 2015). We now propose to compute representative subject-specific constraints for the MD and the AxD derived from single tensor fits in the splenium of the corpus callosum of the particular subject.

Clearly, imposing such constraints on the model is generally not preferred as it precludes the representation of certain variations in diffusion parameters. Even more, the constraints are not required with data acquired at multiple b-values or may be avoided with FLAIR DT imaging. However, these solutions are not applicable to conventional diffusion data collected on a single shell such as ours (see below). A motivation for the constraints is illustrated in figure 2. It displays the AxD (figure 2(A)), radial diffusivity (figure 2(B)) and MD (figure 2(C)) in a white matter segmentation of the brain of a 65 years old male. The histogram in figure 2(D) demonstrates that the MD shows the smallest coefficient of variation across the white matter, which suggests that it may be a suitable constraint. However, assuming a fixed MD in the body of the fornix may not always be appropriate. We therefore also explore constraining the AxD, such that both the FA

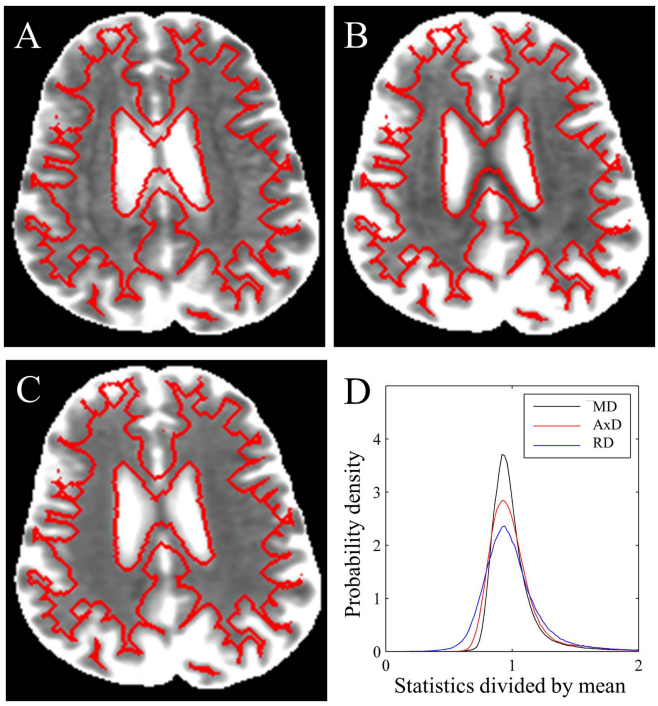

Figure 2. Transversal slices from an asymptomatic 65 years old male brain with contours of a white matter segmentation in red. The white matter segmentation was obtained using a kNN tissue segmentation method (Vrooman *et al* 2007). (A) Axial diffusivity (AxD). (B) Radial diffusivity (RD). (C) Mean diffusivity (MD) of the diffusion tensor. The images are scaled between zero and two times the mean value of each diffusivity statistic. The mean values of AxD, RD and trace are computed from all voxels in the whole-brain white matter segmentation and are 1.1×10^{-3} mm^2 s^{-1}, 0.69×10^{-3} mm^2 s^{-1} and 0.83×10^{-3} mm^2 s^{-1} respectively. (D) Histograms of the AxD, RD and trace after dividing each statistic by its mean value.

and MD in the bi-tensor model can vary across the fornix.

Summarizing, the first constraint assumes a single, fixed MD that may differ per subject, without any further restriction on FA. The second constraint assumes a single, fixed AxD, per subject, without further restrictions on both MD and FA. Subscripts will be used to discriminate between diffusion statistics obtained with different approaches, e.g. FA_{MD} refers to the FA of a bi-tensor model with constrained MD and FA_{AxD} refers to the FA of a bi-tensor model with constrained AxD. Bi-tensor statistics obtained with a global MD-constraint of 8.0×10^{-3} mm^2 s^{-1} will be denoted with the subscript 'MD,Glob', e.g. $FA_{MD,Glob}$. Conventional single tensor statistics will be denoted with the subscript 'ST', e.g. FA_{ST} or MD_{ST}.

2.3. Parameterization of the bi-tensor model

To enforce the constraints, the tissue diffusion tensor **D** in equation (1) is parameterized by a rotation matrix **R** and an eigenvalue matrix **E**, i.e. $\mathbf{D} = \mathbf{RER}^{\mathbf{T}}$. The rotation matrix **R** is a concatenation of three rotations about the *x*-, *y*- and *z*-axes, e.g. $\mathbf{R} = \mathbf{R_x}(\alpha_1)\mathbf{R_y}(\alpha_2)\mathbf{R_z}(\alpha_3)$. The MD-constraint is enforced by parameterizing the eigenvalues of the diagonal matrix **E** as follows:

$$\begin{aligned} \lambda_1 &= 3C_1C_{MD}, \\ \lambda_2 &= 3(1 - C_1)C_2C_{MD}, \\ \lambda_3 &= 3(1 - C_1)(1 - C_2)C_{MD}, \end{aligned} \quad (2)$$

where C_{MD} is the value of the MD constraint and C_1 and C_2 are unknown parameters between 0 and 1. In case of the AxD-constraint, the parameterization is as follows:

$$\begin{aligned} \lambda_1 &= C_{AxD}, \\ \lambda_2 &= C_1C_{AxD}, \\ \lambda_3 &= C_2C_{AxD}, \end{aligned} \quad (3)$$

where C_{AxD} is the value of the AxD-constraint and C_1 and C_2 are again unknown parameters between 0 and 1. In both parametrizations C_1 and C_2 can be constrained during model fitting by an constrained optimization routine.

2.4. Fiber bundle simulations

Phantom fiber bundles were simulated in order to have a reference standard for assessment of features extracted from the single-tensor model and the proposed bi-tensor models. The numeric fiber generator v1.1.1 (Close *et al* 2009) was used to simulate sets of DWIs. Each set contained a single cylindrically shaped white matter fiber bundle of approximately 60 mm in length, with an arbitrary orientation. Diameters of the white matter fiber bundles were varied from 3 to 12 mm in steps of 1.5 mm. Three different microstructures were simulated with respectively FA = {0.75, 0.80, 0.85}, MD = {0.85, 0.80, 0.80} $\times 10^{-3}$ mm^2 s^{-1} and AxD = {1.78, 1.78, 1.89} $\times 10^{-3}$ mm^2 s^{-1}. The white matter bundles

were completely surrounded by CSF, which was modeled as an isotropic compartment with a diffusivity of 3.0×10^{-3} mm^2 s^{-1}. The b_0-intensity of CSF, i.e. imaged at b-value $= 0$ s mm^{-3}, was set to three times the b_0-intensity of the white matter compartment. Acquisition parameters were set to approximately match the acquisition in the Rotterdam Study (Ikram *et al* 2015): 25 gradient directions and a b-value of 1000 s mm^{-2}. PVEs were introduced in the boundary voxels of the fiber bundles, by first generating the DW-MRI signal on a fine imaging grid with a resolution of (0.15 mm)^3 and then summing the signal of each subvoxel element into a coarser voxel grid with a resolution of (3 mm)^3. Finally, Rician distributed data with an SNR of 20 (in the white matter in the b_0-image) were created from the simulated noise-free DWIs. Fiber bundle segmentations were created by including all voxels overlapping the (ground truth) fiber bundle. For each combination of diameter and microstructure, the simulations were conducted ten times such that a mean and standard deviation of relevant diffusion statistics could be computed.

2.5. Study population

Imaging data from the population-based Rotterdam Study was also used to evaluate the proposed framework (Hofman *et al* 2015). The reproducibility of the framework was tested on 20 subjects for whom rescan data (MRI scans acquired on the same scanner) was available (see also (de Boer *et al* 2010)). The mean time between the baseline scan and rescan was 19.5 d (SD 10). These subjects were on average 76.7 (SD 4.8) years old, 50% was female. The framework was further evaluated on a group of 671 subjects, sampled from a cohort of the Rotterdam Study, such that an age distribution from 63 to 80 years was obtained. Due to missing or incorrect fornix segmentations 94 subjects were excluded, as explained below. As such 577 subjects remained: 279 males and 298 females. Ages ranged from 63.9 to 80.0 years, with mean age 69.3 (SD 3.5) years. None of the subjects was diagnosed with dementia. Written informed consent was obtained from all participants.

2.6. Data acquisition

Subjects were scanned on a 1.5 tesla MRI scanner (GE Signa Excite) using an 8-channel head coil. DWIs were acquired with a single shot, diffusion-weighted spin echo echo-planar imaging (EPI) sequence (repetition time $=$ 8575 ms, echo time $=$ 82.6 ms, field of view $=$ 210 mm $\times$ 210 mm, imaging matrix $=$ 96 $\times$ 64 (zero-padded to 256 $\times$ 256), 35 contiguous slices of slice thickness 3.5 mm) in 25 non-collinear directions with a maximum b-value of 1000 s mm^{-2}. Three volumes were acquired without diffusion weighting (the b_0-images). Additionally, structural images were acquired including a T1-weighted sequence (Ikram *et al* 2015).

2.7. Diffusion-image processing

The acquired DWIs were corrected for motion and eddy current distortion by affine coregistration to the reference b_0-image with Elastix (Klein *et al* 2010). Together with the affine transformation, DWIs were upsampled to a 1.0 mm isotropic resolution. Simultaneously, upsampling the image data has little additional adverse effects, but does yield images that are easier to inspect visually for potential artefacts or accurate coregistration. Gradient directions were reoriented according to the rotation component of the affine transformation to maintain correspondence during registration (Leemans and Jones 2009). Next, the single-tensor model, bi-tensor model with global MD-constraint, bi-tensor model with subject-specific MD-constraint and bi-tensor model with subject-specific AxD-constraint were fitted to the DWIs using the fit_MRI toolbox (Poot and Klein 2015) by maximum likelihood estimation assuming Rician distributed data (Gudbjartsson and Patz 1995).

2.8. Corpus callosum segmentation

A segmentation of the splenium of the corpus callosum was applied to obtain a region-of-interest to compute the MD and AxD constraints. For this purpose the Johns Hopkins University (JHU) DTI atlas was registered to the FA images of each subject using a non-rigid transformation with FNIRT, a non-linear registration tool in FSL. The JHU white matter labels, including the splenium of the corpus callosum, were then warped to each subject space using nearest neighbor interpolation. The median MD and AxD of a single tensor fit in the splenium of the corpus callosum segmentation were used as constraints in the fitting of the constrained bi-tensor models.

2.9. Fornix segmentation

Conventional and proposed diffusion statistics of the fornix were compared across subjects. The fornix shows large anatomical variation across different subjects, which hinders accurate registration (Hattori *et al* 2012). As such, a straightforward voxel-based analysis of the fornix in a common (atlas) space was not possible with our data. We therefore chose a region-of-interest based approach in subject space, and used FreeSurfer v5.1 software (Fischl *et al* 2004) to segment the fornix based on T1-weighted images combined with a probabilistic atlas. The FreeSurfer segmentations of the fornix were preferred over tractography segmentations based on the (low-resolution) DWIs, because the higher spatial resolution of the T1-weighted images enabled a more accurate segmentation. Indeed, tractography based segmentations as applied in (Nazem-Zadeh *et al* 2012a, 2012b) largely failed for our data, due to the low resolution of the DWIs.

The FreeSurfer segmentation of the fornix typically contains the body of the fornix (see figures 3(A)

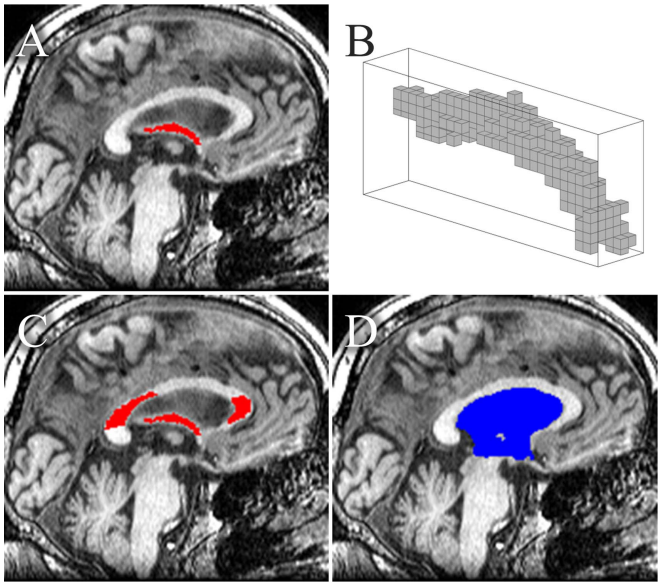

Figure 3. (A) Sagittal slice of a fornix segmentation with T1w background image. (B) Three-dimensional view of a fornix segmentation. Each cube is a $(1\ \text{mm})^3$ voxel. (C) FreeSurfer segmentations of the fornix sometimes erroneously included parts of the corpus callosum, (D) a three-dimensional closing operation applied to the third and lateral ventricles provided a mask that was used to exclude the corpus callosum from fornix segmentations.

and (B)). However, approximately 15% of the fornix segmentations also erroneously included large parts of the corpus callosum (figure 3(C)). The corpus callosum was removed from the fornix segmentations using binary morphology operations as follows. A mask was created by applying a three-dimensional closing operation with a spherical structure element (radius of 4 mm) to the third and lateral ventricles (figure 3(D)). The largest N6-connected structure within this mask was kept as fornix.

To align the fornix segmentation with the DWIs, a transformation was computed by rigidly coregistering the T1-weighted scan to the b_0-image using FLIRT, a linear registration tool in FSL. However, EPI acquisitions are very sensitive to static magnetic field inhomogeneities. Variations in the static magnetic field, particularly at air-tissue interfaces, induce geometric distortions in the b_0-image due to the EPI readout. A straightforward rigid registration tends to slightly misalign the fornix to correct for geometric distortions elsewhere in the brain. This misalignment was prevented by using a smoothed FreeSurfer segmentation of the third and lateral ventricles as a weighting image for the cost function in FLIRT. Essentially, this emphasized accurate registration of the region around the fornix. All fornix segmentations were inspected and 94 out of 671 subjects with missing or incorrect fornix segmentations were removed from the study. More specifically; in 17 subjects FreeSurfer crashed, in 61 subjects FreeSurfer did not label a single voxel as fornix, and in 16 subjects the fornix segmentation contained major defects.

3. Results

3.1. Example of a typical subject

A typical result for a 65 year old brain is displayed in figure 4. Figure 4(A) shows a coronal slice of a T1-weighted scan with the fornix segmentation in red. The small size of the fornix can be appreciated, e.g. even the body the thickest part of the fornix, is only 4-5 mm in diameter. In figures 4(B)–(E), the FA_{ST}, MD_{ST}, FA_{MD} and f_{MD} are shown respectively. For visualization purposes voxels with tissue fraction f_{MD} smaller than 0.3 have been masked black in figure 4(D). In these voxels the MRI signal from the tissue compartment is too small for reliable estimation of FA_{MD}. Furthermore, observe that the image contrast provided by MD_{ST} is approximately the inverse of the image contrast provided by f_{MD}. Due to the constraint in the bi-tensor model, any increase in the MD in a voxel is explained by a decrease in f_{MD}

3.2. Simulated fiber bundles

The segmented voxels in the simulated fiber bundle are affected by various degrees of CSF contamination, e.g. boundary voxels are typically more contaminated than center voxels. The effects of CSF contamination can be reduced by excluding the most contaminated voxels from the analysis. We therefore considered three (arbitrarily chosen) levels of contamination at which to extract diffusivity statistics from the segmentations, by computing an average over all voxels, over the 50% least contaminated voxels, and over the 10% least contaminated voxels. The ground truth degree of

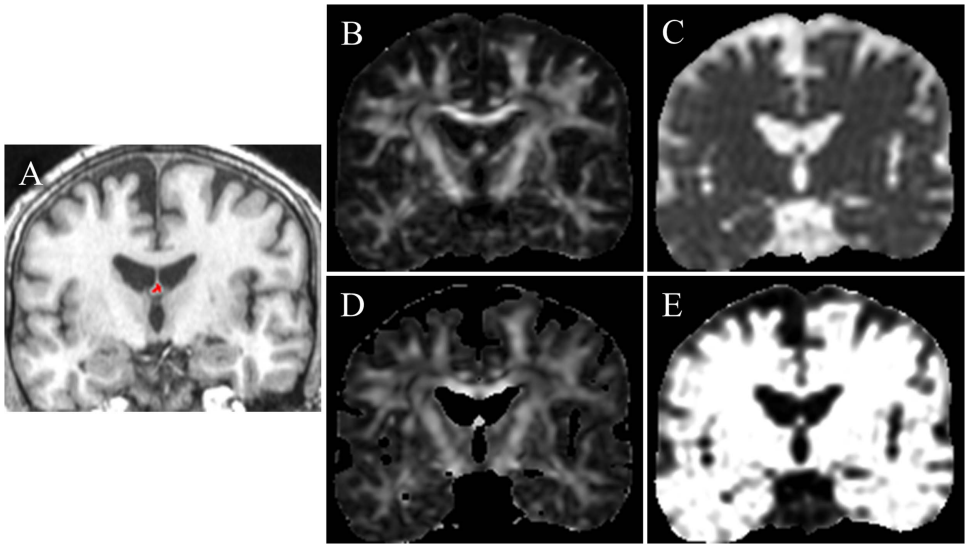

Figure 4. Coronal slices from an asymptomatic 65 year old male brain. (A) T1w-image with fornix segmentation in red. (B) FA_{ST}. (C) MD_{ST}. (D) FA_{MD} (voxels with $f_{MD} < 0.3$ have been masked black). (E) f_{MD}.

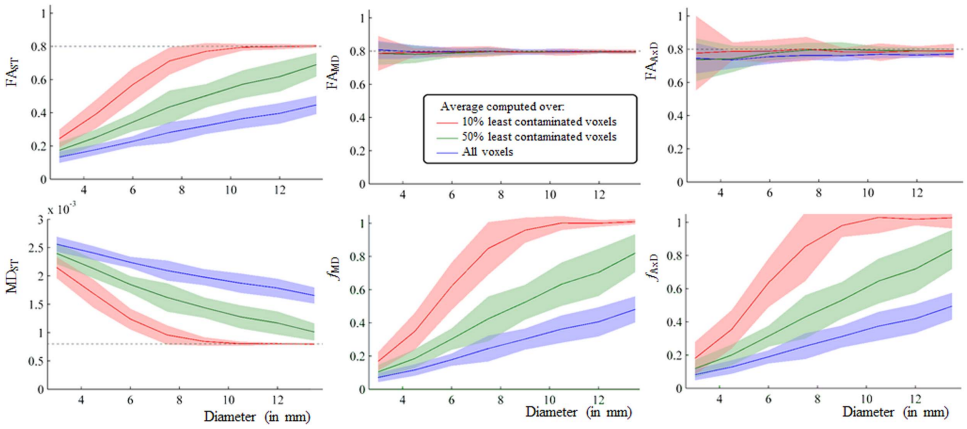

Figure 5. Effect of selecting the least contaminated voxels within tract segmentations of CSF-contaminated fiber bundles. Diffusion properties from single fiber bundle configurations with FA = 0.8 and different fiber bundle diameters were estimated with the single-tensor model (left column), the bi-tensor model with constrained mean diffusivity (middle column), and the bi-tensor model with constrained axial diffusivity (right column). Diffusivity statistics were extracted by taking an average over all voxels (blue), over the 50% least contaminated voxels (green), and over the 10% least contaminated voxels (red). The shaded areas represent two standard errors around the mean values; the gray dashed lines represent the simulated ground truth.

CSF contamination in each voxel was computed from the (noiseless) b_0-image.

Using the three exclusion levels, the FA and MD of a single tensor model (FA_{ST} and MD_{ST}) as well as the FA and tissue fraction f of the bi-tensor model with constrained MD (FA_{MD} and f_{MD}) and constrained AxD (FA_{AxD} and f_{AxD}), are plotted against the diameter of the simulated fiber bundles in figure 5. The shaded areas along the plotted curves represent two standard errors around the mean values. The constraints were set to $C_{MD} = 0.8 \times 10^{-3}\,mm^2\,s^{-1}$ and $C_{AxD} = 1.78 \times 10^{-3}\,mm^2\,s^{-1}$ in respectively the MD constrained and AxD constrained bi-tensor model. Note that the ground truth values in the simulated fiber bundle has an FA of 0.8.

It can be observed that conventional diffusion statistics (FA_{ST} and MD_{ST}) and the bi-tensor tissue fractions (f_{MD} and f_{AxD}) become increasingly biased with decreasing simulated fiber diameter and with higher percentages of contaminated voxels included. Obviously, computing the average from the 10% least contaminated voxels yields the smallest bias with respect to the simulated ground truth. At this exclusion level, the extracted FA_{ST} and MD_{ST} are almost equal to their simulated ground truth in fiber bundles with diameters larger than 9 mm (i.e. three times the voxel size). This is not the case in fiber bundles with smaller diameters, or when the average is computed from the more contaminated voxels in the tract segmentations. Furthermore, the CSF contamination

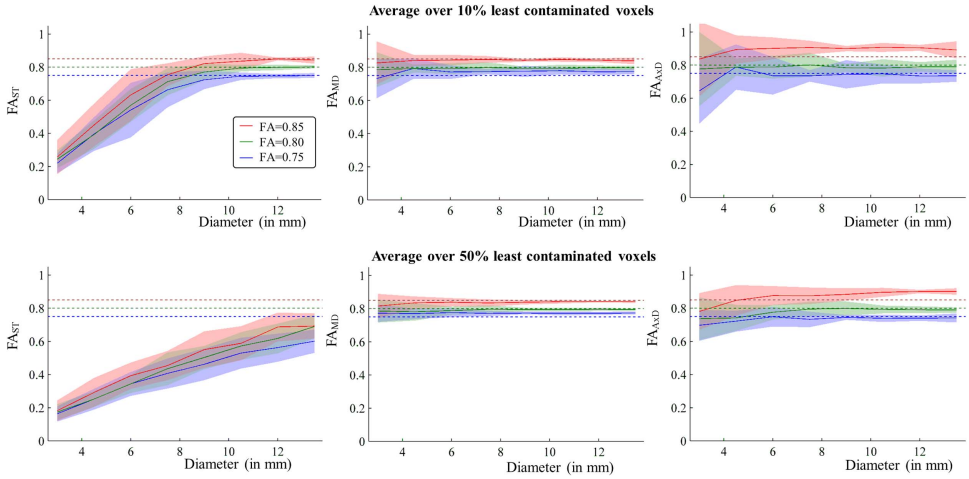

Figure 6. Impact of CSF contamination on fiber bundle configurations with varying diameters and FA. Diffusion properties from single fiber bundle configurations with different FA and different diameters were estimated with the single-tensor model (left column), the bi-tensor model with constrained mean diffusivity (middle column), and the bi-tensor model with constrained axial diffusivity (right column). Diffusivity statistics were computed by taking an average over the 10% least contaminated voxels (top row), or over the 50% least contaminated voxels (bottom row). The shaded areas represent two standard errors around the mean values; the colored dashed lines represent the simulated ground truth.

introduces a relatively large uncertainty in the estimated conventional diffusion statistics (FA_{ST} and MD_{ST}) and the bi-tensor tissue fractions (f_{MD} and f_{AxD}).

The mean CSF contamination-invariant statistics FA_{MD} and FA_{AxD} appear independent of fiber bundle diameter and the used exclusion level and are approximately equal to the simulated ground truth. In the smallest fiber bundle the uncertainties in estimated FA_{MD} and FA_{AxD} are a little larger than ten percent of the ground truth. This can be explained by a smaller region-of-interest over which these statistics are computed, and (on average) a smaller fraction of the signal that originates from the tissue compartment in each voxel. Furthermore, the variation in FA_{AxD} appears larger than the variation in FA_{MD}.

Subsequently, the ability to discriminate between fiber bundle configurations with varying FA was evaluated using the 10% and 50% least contaminated voxels. For fiber bundles with different simulated FA values (0.75, 0.8 and 0.85), conventional and proposed diffusion statistics are plotted against the diameter in figure 6. The overlapping confidence bounds of FA_{ST} for bundles smaller than 9.0 mm as well as the dependency of FA_{ST} on bundle diameter imply that bundles with these differences in FA cannot be distinguished. In fiber bundles with diameters of 6.0 mm and larger, the variance in both FA_{MD} and FA_{AxD} is sufficiently small to discriminate between the three simulated FA's.

In figure 6 the effect of a mismatch between the applied constraints and the ground truth can be observed. The fiber bundle with true FA = 0.75 has true MD = 0.85×10^{-3} mm^2 s^{-1}, whereas the applied MD-constraint was $C_{MD} = 0.80 \times 10^{-3}$ mm^2 s^{-1}. In the second column of figure 6 it is shown that in this case the FA_{MD} slightly overestimates the true FA by approximately 5%. Observe, however, that despite the bias, the mean FA_{MD} is still independent of fiber diameter. Similarly, the fiber bundle with true FA = 0.85 has true AxD = 1.89×10^{-3} mm^2 s^{-1}, whereas the applied AxD-constraint was $C_{AxD} = 1.78 \times 10^{-3}$ mm^2 s^{-1}. In the third column of figure 6 it can be observed that FA_{AxD} slightly overestimates the true FA in this situation by about 5%.

3.3. Reproducibility study

As demonstrated in the simulations, excluding the most contaminated voxels from the segmentation is a straightforward method to reduce the effects of CSF contamination. Unfortunately the ground-truth contamination level is not known for our clinical datasets. Instead, we selected the 10% and 50% voxels with the highest FA_{ST} in the fornix segmentation of our clinical datasets.

On 20 subjects for whom rescan data was available, we evaluated the reproducibility of parameter estimation. Baseline and follow-up scans were processed using the described processing pipeline. The mean FA_{ST}, MD_{ST}, $FA_{MD,Glob}$, FA_{MD}, FA_{AxD}, and tissue fractions $f_{MD,Glob}$, f_{MD} and f_{MD} in the 10% and 50% highest FA_{ST} voxels of the fornix were computed for both scans of all twenty subjects. For all diffusion statistics, Bland–Altman plots showing the difference between the time point measurements as function of the mean are presented in figure 7. Diffusion statistics computed from the 10% highest FA_{ST} voxels are displayed in red, diffusion statistics computed from the 50% highest FA_{ST} voxels are displayed in blue. The coefficients of repeatability (CR), defined as the 1.96 times the

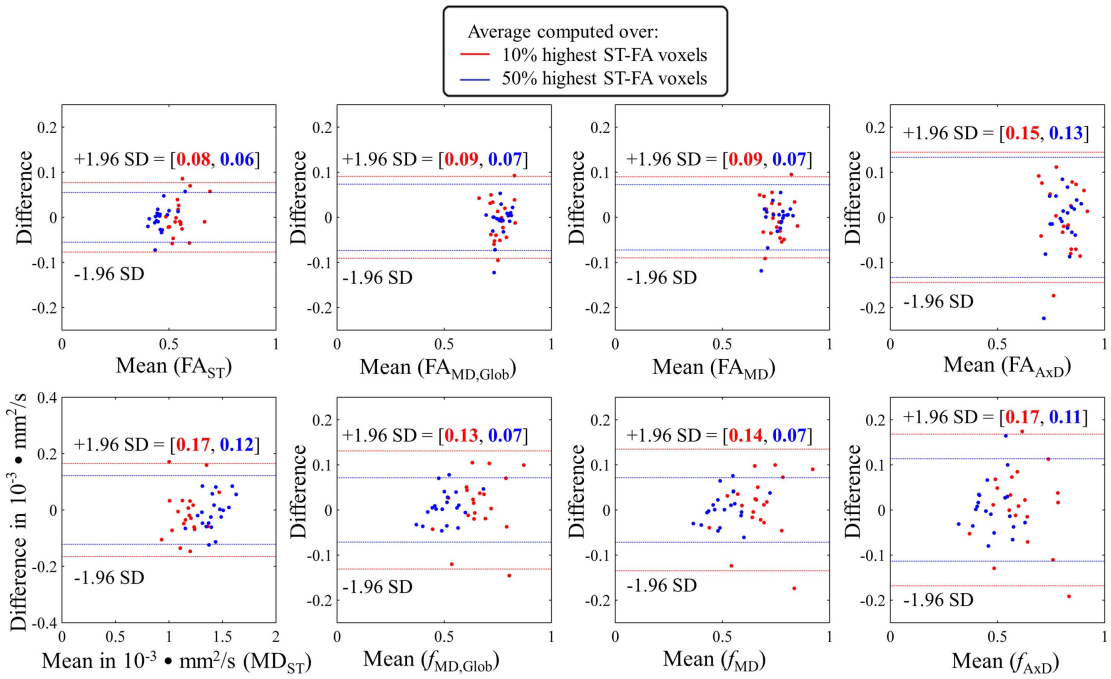

Figure 7. Bland–Altman plots show the repeatability of estimating the mean FA_{ST}, MD_{ST}, $FA_{MD,Glob}$, FA_{MD}, FA_{AxD}, and tissue fractions $f_{MD,Glob}$, f_{MD} and f_{MD} from the 10% highest (in red) or the 50% highest (in blue) FA_{ST} voxels in the fornix. The diffusivity statistics were estimated from baseline and follow-up scans in twenty subjects of the Rotterdam Study for whom rescan data was available.

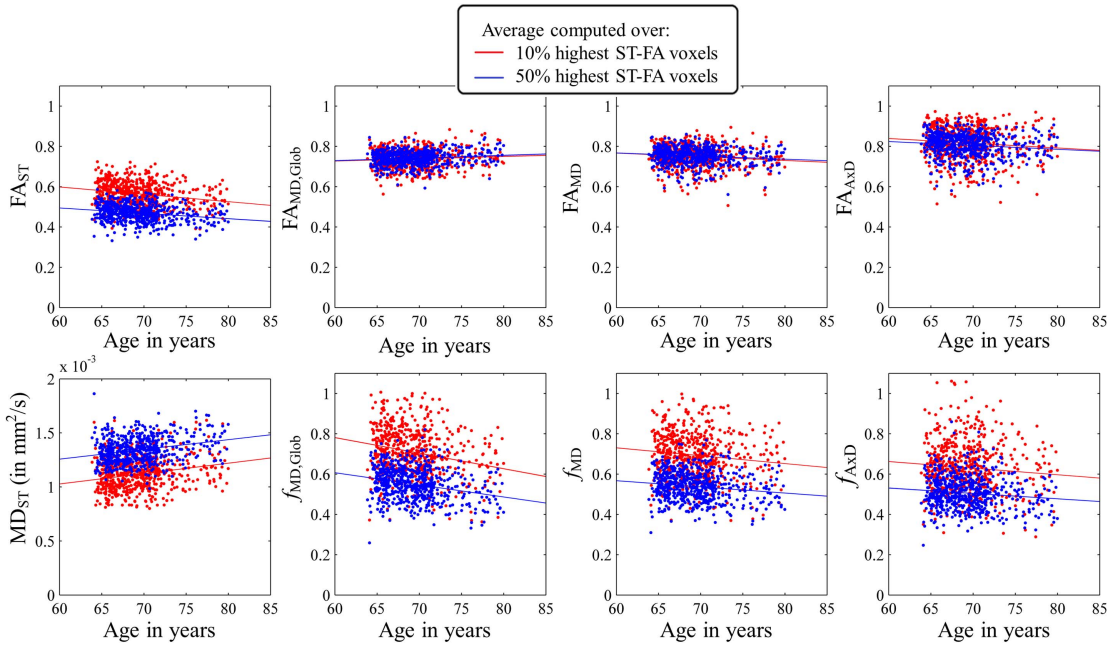

Figure 8. Scatter plots of diffusion statistics FA_{ST}, MD_{ST}, $FA_{MD,Glob}$, FA_{MD}, FA_{AxD}, $f_{MD,Glob}$, f_{MD} and f_{AxD} versus age for 577 subjects of the Rotterdam study. Statistics computed from the 10% highest FA_{ST} voxels in the fornix are shown in red, from the 50% highest FA_{ST} voxels in blue. Linear regression lines with age are shown in each plot.

standard deviation of the differences between the two measurements are also reported in figure 7. For all diffusion statistics the CR is smallest when the 50% highest FA_{ST} voxels are used, but including more contaminated voxels also decreases the mean FA_{ST} and increases MD_{ST}, while f_{MD} and f_{AxD} both decrease.

3.4. Ageing study

Figure 8 shows scatter plots of the estimated FA_{ST}, MD_{ST}, $FA_{MD,Glob}$, FA_{MD}, FA_{AxD}, $f_{MD,Glob}$, f_{MD} and f_{AxD} in the body of the fornix versus age. Linear regression lines with age were computed for all diffusion statistics. Red points and regression lines

Table 1. Regression coefficients for diffusion statistics from figure 8. Column β_{age} (10%) shows the regression coefficients of statistics computed from the 10% highest FA_{ST} voxels in the fornix, column β_{age} (50%) of the 50% highest FA_{ST} voxels in the fornix. In row $FA_{MD}{}^{*}$ and $f_{MD}{}^{*}$ the regression coefficient were calculated including the used MD-constraint (i.e. $MD_{Splenium}$) as a covariate. In row $FA_{AxD}{}^{*}$ and $f_{AxD}{}^{*}$ the regression coefficient were calculated including the used AxD-constraint (i.e. $AxD_{Splenium}$) as a covariate. The unit of β is in yr^{-1}, except for MD_{ST}, which is in $mm^2\,s^{-1}\,yr^{-1}$. Regression coefficients with a p-value < 0.05 are denoted in bold.

Variables	β_{age} (10%)	p-value	β_{age} (50%)	p-value
FA_{ST}	$\mathbf{-3.6 \times 10^{-3}}$	1.3×10^{-7}	$\mathbf{-2.7 \times 10^{-3}}$	1.3×10^{-7}
MD_{ST}	$\mathbf{9.6 \times 10^{-6}}$	4.1×10^{-8}	$\mathbf{9.0 \times 10^{-6}}$	1.2×10^{-10}
$FA_{MD,Glob}$	$\mathbf{1.1 \times 10^{-3}}$	4.6×10^{-2}	$\mathbf{1,3 \times 10^{-3}}$	2.1×10^{-3}
$f_{MD,Glob}$	$\mathbf{-7.7 \times 10^{-3}}$	5.4×10^{-8}	$\mathbf{-6.0 \times 10^{-3}}$	1.5×10^{-10}
FA_{MD}	$\mathbf{-1.8 \times 10^{-3}}$	3.9×10^{-3}	$\mathbf{-1.5 \times 10^{-3}}$	2.8×10^{-3}
FA_{AxD}	$\mathbf{-2.4 \times 10^{-3}}$	1.7×10^{-2}	$\mathbf{-1.9 \times 10^{-3}}$	6.0×10^{-3}
f_{MD}	$\mathbf{-3.9 \times 10^{-3}}$	2.9×10^{-3}	$\mathbf{-3.1 \times 10^{-3}}$	3.0×10^{-4}
f_{AxD}	$\mathbf{-3.3 \times 10^{-3}}$	3.3×10^{-2}	$\mathbf{-2.7 \times 10^{-3}}$	5.3×10^{-3}
$FA_{MD}{}^{*}$	7.3×10^{-4}	2.2×10^{-1}	$\mathbf{9.0 \times 10^{-4}}$	4.6×10^{-2}
$FA_{AxD}{}^{*}$	5.2×10^{-4}	6.0×10^{-1}	4.1×10^{-4}	5.6×10^{-1}
$f_{MD}{}^{*}$	$\mathbf{-3.9 \times 10^{-3}}$	5.6×10^{-3}	$\mathbf{-3.1 \times 10^{-3}}$	6.4×10^{-4}
$f_{AxD}{}^{*}$	$\mathbf{-3.8 \times 10^{-3}}$	2.0×10^{-2}	$\mathbf{-3.0 \times 10^{-3}}$	3.4×10^{-3}

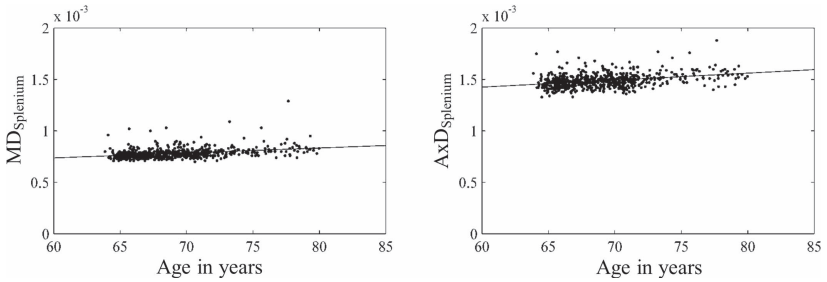

Figure 9. Scatter plots of diffusion statistics of the median FA_{ST} (left) and MD_{ST} (right) versus age in the splenium of the corpus callosum. Linear regression lines with age are also shown. All regression lines are significant.

represent statistics computed from the 10% highest FA_{ST} voxels, blue points and regression lines represent statistics computed from the 50% highest FA_{ST} voxels. The regression-coefficients of these lines and their p-values are reported in table 1. All regression coefficients are significantly different from zero, both for the statistics computed from the 10% and 50% highest FA_{ST} voxels.

Observe that diffusion statistics FA_{ST}, FA_{MD} and FA_{AxD} all decrease with age, whereas $FA_{MD,Glob}$ increases with age (with a very small slope). Furthermore, MD_{ST} increases with age and the tissue fractions $f_{MD,Glob}$, f_{MD} and f_{AxD} all decrease with age. For conventional diffusion statistics (i.e. FA_{ST} and MD_{ST}) and bi-tensor tissue fractions $f_{MD,Glob}$, f_{MD} and f_{AxD}, a clear difference can be observed between the statistics computed from the 10% and 50% highest FA_{ST} voxels. A paired sample t-test confirmed these differences were all significant with p-values smaller than 1×10^{-10}. The diffusion statistics $FA_{MD,Glob}$, FA_{MD} and FA_{AxD} provide similar values in the 10% and 50% highest FA_{ST} voxels.

The MD and the AxD of the splenium of the corpus callosum were used as constraints in the bi-tensor model. Scatter plots of MD and AxD in the splenium versus age have been visualized in figure 9. For both statistics the linear regression line with age increases significantly. To investigate whether this increase explains the observed changes in the fornix, we included the MD of the splenium as a covariate in our regression analysis of FA_{MD} and f_{MD} with age. In a similar fashion the AxD of the splenium was included in our regression analysis of FA_{AxD} and f_{AxD} with age. The results are reported in table 1. Here it can be seen that after correction the bi-tensor tissue fractions f_{MD} and f_{AxD} still decrease significantly with age. However, both FA_{MD} and FA_{AxD} no longer correlate significantly with age, except for FA_{MD} that increases with age when computed from the 50% highest FA_{ST} voxels (although the slope is rather small).

4. Discussion

We have presented and evaluated a framework that can be used to compute CSF contamination-invariant statistics in the body of the fornix from conventionally acquired DWIs.

4.1. Dependence on macrostructural properties

The simulation results showed that conventional, single-tensor, DTI metrics such as FA_{ST} and MD_{ST} become increasingly biased with decreasing fiber diameter. This confirms prior work that investigated the influence of PVE on DTI metrics (Vos *et al* 2011). Our simulation experiment also demonstrated that excluding the most contaminated voxels from the fiber bundle segmentations was only partially effective in removing CSF contamination. In fiber bundles with diameters larger than approximately three times the voxel size, CSF contamination could be removed by restricting the analysis to the 10% least contaminated voxels. Segmentations of smaller fiber bundles exist (almost) exclusively of boundary voxels, for which the employed heuristic of analyzing the 10% least contaminated voxels was less effective. Essentially, this demonstrates that the conventional FA measurements on the fornix in elderly subjects (having a diameter of approximately 4 mm) can be particularly affected by CSF contamination when imaged with a slice thickness or in-plane resolution larger than 3 mm.

The mean FA_{MD} and FA_{AxD} were independent of the fiber diameter even for very small fiber diameters. However, for small fiber diameters (i.e. smaller than 6 mm) the variance in the estimated FA_{MD} and FA_{AxD} increased a bit due to a smaller region-of-interest over which these statistics are computed, and (on average) a smaller fraction of the signal that originates from the tissue compartment in each voxel.

The macrostructural dependence of diffusion statistics was further evaluated on the aging study data by comparing the diffusion statistics computed from respectively the 10% and 50% highest FA_{ST} voxels. For conventional diffusion statistics such as FA_{ST} and MD_{ST}, clear and highly significant differences were observed between the means from the 10% and 50% highest FA_{ST} voxels. Diffusion statistics FA_{MD} and FA_{AxD} appeared relatively robust to the choice of using the 10% or 50% highest FA_{ST} voxels, suggesting these statistics are CSF contamination-invariant.

4.2. Ageing

Conventional diffusion statistics FA_{ST} and MD_{ST} decreased and increased, respectively, with age. This may reflect changes in the fornix microstructure, but may also reflect fornix atrophy that yields increased levels of CSF contamination. The bi-tensor statistics FA_{MD} and FA_{AxD} both decreased significantly with age, suggesting changes in the fornix microstructure. However, the negative correlation of FA_{MD} and FA_{AxD} with age disappeared when the applied subject-specific constraints were added as a covariate in the regression analysis. This may suggest that the microstructural change in the body of the fornix is not significantly different from the microstructural change in the splenium of the corpus callosum.

The bi-tensor tissue fractions f_{MD} and f_{AxD} decreased significantly with age, even after adding the applied subject-specific constraints as a covariate in the regression analysis. This may suggest that there is a change in the fornix that appears as if tissue is being replaced by water. This could be due to fornix atrophy but could also reflect a higher degree of extra-cellular water in the fornix microstructure (see below).

4.3. Subject-specific constraints versus a global constraint

The use of subject-specific constraints has advantages and disadvantages compared to the use of a global constraint. By computing subject-specific constraints from (noisy) splenium data, additional uncertainty may be added to the estimated bi-tensor parameters compared to a global constraint. However, the results of the reproducibility study showed that the reproducibility of $FA_{MD,Glob}$ and FA_{MD} is very similar, which suggests this effect is not large. An advantage of subject-specific constraints is that computing the constraints from the same subject may yield an increased accuracy of the estimated bi-tensor parameters. Particularly in a study population with large variations (e.g. due to a wide age range), the use of a global constraint may not be appropriate for every subject. This may result in a decreased accuracy compared to using subject-specific constraints.

4.4. Limitations

Inherent limitations of our work are in the constraints that have to be imposed to make estimation with the bi-tensor well-posed in the fornix. Besides bias and variance due to noise on the data, also potential differences in the tissue microstructure of the splenium and fornix (e.g. different degrees of extracellular water) may make the imposed constraints less appropriate. The effect of using inappropriate constraints was evaluated in simulated fiber bundles. The results showed that when these constraints are violated, a slight bias may be introduced into the estimation of FA_{MD} and FA_{AxD}. However, for realistic in-vivo differences between ground truth and constrained value these biases were small (in the order of 5%). Still, these effects may add scatter to the final data, thereby decreasing the statistical power of the proposed framework with respect to single-tensor data.

One type of microstructural change that may not be reflected in the FA of a bi-tensor model is an increase in extracellular, intra-tract water content. The CSF-compartment in the bi-tensor model is a free-water compartment. Simultaneously, in loosely packed white matter bundles, extracellular water in the microstructure could be assumed to have diffusivity properties close to those of free-water. Under this assumption any increase in extracellular water gives rise to a decrease in the tissue fraction, while leaving the diffusivities of the tissue diffusion tensor

unchanged. As a consequence, the tissue fractions in the bi-tensor model are not CSF-contamination invariant: it may model the amount of CSF contamination as well as the amount of extracellular water. Thus, the interpretation of changes in this parameter is not trivial as it may be driven by both macrostructural and microstructural changes. To further distinguish between these different kinds of microstructural change an acquisition protocol with multiple *b*-values is required. However, such imaging was not performed for our study data.

5. Conclusion

Our research showed how conventional (single non-zero *b*-value) DW-MRI datasets can be analyzed with an MD-constrained or AxD-constrained bi-tensor model. In simulations the mean FA estimated by these constrained bi-tensors models did not depend on macrostructural properties, which suggests that our diffusion statistics are indeed CSF contamination-invariant. Diffusion parameters such as the bi-tensor tissue fractions or the single tensor FA or MD were not CSF contamination-invariant. The bias in these diffusion statistics did not only depend on macrostructural properties such as the diameter of a white matter structure, but also on whether the 10% or 50% least contaminated voxels in a segmentation were used. Results from the ageing study suggest the occurrence of microstructural change in the body of the fornix with age. However, this change is not significantly different from the microstructural change occurring in the splenium of the corpus callosum. In conclusion, the distinction of an isotropic and an anisotropic diffusion compartment can allow a more sophisticated analysis in future studies of the fornix, particularly to discriminate between microstructural and macrostructural changes.

Acknowledgments

This study was financially supported as part of the STW Perspectief programme Population Imaging Genetics (ImaGene) supported by the Dutch Technology Foundation (STW), project 12722.

References

Aggleton J P, Mcmackin D, Carpenter K, Hornak J, Kapur N, Halpin S, Wiles C, Kamel H, Brennan P and Carton S 2000 Differential cognitive effects of colloid cysts in the third ventricle that spare or compromise the fornix *Brain* **123** 800–15

Alexander A L, Hasan K M, Lazar M, Tsuruda J S and Parker D L 2001 Analysis of partial volume effects in diffusion-tensor MRI *Magn. Reson. Med.* **45** 770–80

Arkesteijn G A, Poot D H, De Groot M, Vernooij M W, Niessen W J, Van Vliet L J and Vos F M 2015 CSF contamination-invariant statistics in diffusion-weighted MRI *2015 IEEE 12th Int. Symp. on Biomedical Imaging (ISBI)* (Piscataway, NJ: IEEE) pp 454–7

Basser P J, Mattiello J and Lebihan D 1994 MR diffusion tensor spectroscopy and imaging *Biophys. J.* **66** 259–67

Beaulieu C 2002 The basis of anisotropic water diffusion in the nervous system—a technical review *NMR Biomed.* **15** 435–55

Chou M-C, Lin Y-R, Huang T-Y, Wang C-Y, Chung H-W, Juan C-J and Chen C-Y 2005 FLAIR diffusion-tensor MR tractography: comparison of fiber tracking with conventional imaging *Am. J. Neuroradiol.* **26** 591–7

Close T G, Tournier J-D, Calamante F, Johnston L A, Mareels I and Connelly A 2009 A software tool to generate simulated white matter structures for the assessment of fibre-tracking algorithms *NeuroImage* **47** 1288–300

Concha L, Gross D W and Beaulieu C 2005 Diffusion tensor tractography of the limbic system *Am. J. Neuroradiol.* **26** 2267–74

de Boer R, Vrooman H A, Ikram M A, Vernooij M W, Breteler M M, Van Der Lugt A and Niessen W J 2010 Accuracy and reproducibility study of automatic MRI brain tissue segmentation methods *Neuroimage* **51** 1047–56

Fischl B, Salat D H, Van Der Kouwe A J, Makris N, Ségonne F, Quinn B T and Dale A M 2004 Sequence-independent segmentation of magnetic resonance images *Neuroimage* **23** S69–84

Gudbjartsson H and Patz S 1995 The Rician distribution of noisy MRI data *Magn. Reson. Med.* **34** 910–4

Hattori T, Ito K, Aoki S, Yuasa T, Sato R, Ishikawa M, Sawaura H, Hori M and Mizusawa H 2012 White matter alteration in idiopathic normal pressure hydrocephalus: tract-based spatial statistics study *Am. J. Neuroradiol.* **33** 97–103

Hofman A, Brusselle G G, Murad S D, Van Duijn C M, Franco O H, Goedegebure A, Ikram M A, Klaver C C, Nijsten T E and Peeters R P 2015 The Rotterdam study: 2016 objectives and design update *Eur. J. Epidemiol.* **30** 661–708

Hoy A R, Koay C G, Kecskemeti S R and Alexander A L 2014 Optimization of a free water elimination two-compartment model for diffusion tensor imaging *NeuroImage* **103** 323–33

Ikram M A, Van Der Lugt A, Niessen W J, Koudstaal P J, Krestin G P, Hofman A, Bos D and Vernooij M W 2015 The Rotterdam scan study: design update 2016 and main findings *Eur. J. Epidemiol.* **30** 1299–315

Jack C R, Bernstein M A, Borowski B J, Gunter J L, Fox N C, Thompson P M, Schuff N, Krueger G, Killiany R J and Decarli C S 2010 Update on the magnetic resonance imaging core of the Alzheimer's disease neuroimaging initiative *Alzheimer's Dementia* **6** 212–20

Klein S, Staring M, Murphy K, Viergever M and Pluim J P 2010 Elastix: a toolbox for intensity-based medical image registration *IEEE Trans. Med. Imaging* **29** 196–205

Leemans A and Jones D K 2009 The *B*-matrix must be rotated when correcting for subject motion in DTI data *Magn. Reson. Med.* **61** 1336–49

Metzler-Baddeley C, Jones D K, Belaroussi B, Aggleton J P and O'sullivan M J 2011 Frontotemporal connections in episodic memory and aging: a diffusion MRI tractography study *J. Neurosci.* **31** 13236–45

Metzler-Baddeley C, Jones D K and O'sullivan M J 2014 CSF contamination contributes to apparent microstructural alterations in mild cognitive impairment *Neuroimage* **92** 27–35

Metzler-Baddeley C, O'sullivan M J, Bells S, Pasternak O and Jones D K 2012 How and how not to correct for CSF-contamination in diffusion MRI *NeuroImage* **59** 1394–403

Nazem-Zadeh M-R, Chapman C H, Lawrence T L, Tsien C I and Cao Y 2012a Radiation therapy effects on white matter fiber tracts of the limbic circuit *Med. Phys.* **39** 5603–13

Nazem-Zadeh M-R, Saksena S, Babajani-Fermi A, Jiang Q, Soltanian-Zadeh H, Rosenblum M, Mikkelsen T and Jain R 2012b Segmentation of corpus callosum using diffusion tensor imaging: validation in patients with glioblastoma *BMC Med. Imaging* **12** 10

Papadakis N G, Martin K M, Mustafa M H, Wilkinson I D, Griffiths P D, Huang C L H and Woodruff P W 2002 Study of the effect of CSF suppression on white matter diffusion anisotropy mapping of healthy human brain *Magn. Reson. Med.* **48** 394–8

Pasternak O, Sochen N, Gur Y, Intrator N and Assaf Y 2009 Free water elimination and mapping from diffusion MRI *Magn. Reson. Med.* **62** 717–30

Pierpaoli C and Jones D 2004 Removing CSF contamination in brain DT-MRIs by using a two-compartment tensor model *Proc. Int. Society for Magnetic Resonance in Medicine 12th Scientific Meeting ISMRM04* p 1215

Poot D H and Klein S 2015 Detecting statistically significant differences in quantitative MRI experiments, applied to diffusion tensor imaging *IEEE Trans. Med. Imaging* **34** 1164–76

Rashid W, Hadjiprocopis A, Griffin C, Chard D, Davies G, Barker G, Tofts P, Thompson A and Miller D 2004 Diffusion tensor imaging of early relapsing-remitting multiple sclerosis with histogram analysis using automated segmentation and brain volume correction *Multiple Sclerosis* **10** 9–15

Stejskal E and Tanner J 1965 Spin diffusion measurements: spin echoes in the presence of a time-dependent field gradient *J. Chem. Phys.* **42** 288–92

Takao H, Hayashi N, Inano S and Ohtomo K 2011 Effect of head size on diffusion tensor imaging *Neuroimage* **57** 958–67

Taquet M, Scherrer B, Boumal N, Peters J M, Macq B and Warfield S K 2015 Improved fidelity of brain microstructure mapping from single-shell diffusion MRI *Med. Image Anal.* **26** 268–86

Vernooij M W, De Groot M, Van Der Lugt A, Ikram M A, Krestin G P, Hofman A, Niessen W J and Breteler M M 2008 White matter atrophy and lesion formation explain the loss of structural integrity of white matter in aging *Neuroimage* **43** 470–7

Vos S B, Jones D K, Viergever M A and Leemans A 2011 Partial volume effect as a hidden covariate in DTI analyses *Neuroimage* **55** 1566–76

Vrooman H A, Cocosco C A, Van Der Lijn F, Stokking R, Ikram M A, Vernooij M W, Breteler M M and Niessen W J 2007 Multi-spectral brain tissue segmentation using automatically trained *k*-nearest-neighbor classification *Neuroimage* **37** 71–81

Zhang H, Schneider T, Wheeler-Kingshott C A and Alexander D C 2012 NODDI: practical *in vivo* neurite orientation dispersion and density imaging of the human brain *Neuroimage* **61** 1000–16